UNIVERSITY
OF TRENTO

DIPARTIMENTO DI INGEGNERIA E SCIENZA DELL'INFORMAZIONE

38123 Povo – Trento (Italy), Via Sommarive 14
http://www.disi.unitn.it

ITERATIVE IMAGE RECONSTRUCTION OF TWO-DIMENSIONAL SCATTERERS ILLUMINATED BY TE WAVES

D. Franceschini, M Donelli, G. Franceschini, and A. Massa

January 2011

Technical Report # DISI-11-081

Iterative Image Reconstruction of Two-dimensional Scatterers Illuminated by TE Waves

Davide Franceschini, Massimo Donelli, Gabriele Franceschini, and Andrea Massa

Abstract

The iterative reconstruction of unknown objects from TE measured scattered field data is presented. The paper investigates the performance of the iterative multiscaling approach (IMSA) in exploiting transverse electric (TE) illuminations. As a matter of fact, in these conditions, the problem turns out to be more complicated than the TM scalar one in terms of mathematical model as well as computational costs. However, it is expected that more information on the scenario under test can be drawn from scattered data. Therefore, this work is aimed at verifying whether the TE case can provide additional information on the scenario under test (compared to the TM illumination) and how such an enhancement can be suitably exploited by the IMSA for improving the reconstruction accuracy of the retrieval process. Such an analysis will be carried out by means of a set of numerical experiments concerned with dielectric and metallic targets in single and multiple objects configurations. Synthetic as well as experimental data will be dealt with.

Index Terms

Microwave Imaging, Electromagnetic Scattering, Inverse Problems, Multiresolution Technique, TE Illumination.

I. Introduction

The reconstruction of inaccessible areas has been addressed employing electromagnetic fields at microwave frequencies in a wide number of applications (see [1][2][3][4]). The imaging of the unknown targets is generally achieved through a suitable processing of the field data collected away from the scatterers. Moreover, the exploitation of the complex scattering phenomena allows a quantitative description of the dielectric and conductivity distributions of the domain under test.

In this framework, two main categories of methodological approaches have been developed. The first class concerns with approximate techniques, such as the physical optic methods [5][6] and the Born and Rytov approximations [7][8]. These approaches simplify the imaging problem by considering some approximations, but also limit the range of retrievable profiles. A second class of methods aims at rigorously solving the nonlinear inverse scattering equations, usually reformulating the original problem into an optimization one [9][10][11] [12][13][14][15]. Such approaches extend the range of retrievable objects but they also make the reconstruction problem more troublesome and computationally expensive since the arising non-linearity and ill-posedness have to be suitably addressed.

Moreover, although many efforts (see for example [16], [17], [18] and [19]) have been addressed to develop effective methods for 3D reconstructions, tomographic configurations are generally considered if possible, since the dimensionality of the problem requires less computational load.

Furthermore, the inverse scattering problem is generally simplified by considering suitable illumination conditions. The most widely adopted polarization is the transverse magnetic (TM) one, where the incident electric field is directed along the invariance axis of the cylindrical geometry. Such a situation allows to reformulate the original vectorial problem by means of scalar relations, thus reducing the overall complexity of the mathematical model and the arising computational burden needed for its numerical solution.

On the other hand, dealing with a transverse electric (TE) illumination (where the magnetic field is polarized along the axis of the cylinder) requires a more complex mathematical description since the arising vectorial integral equations present derivatives of both the background Green's function and the field [20]. Nevertheless, since TM and TE cases are physically uncoupled,

D. Franceschini, M. Donelli, G. Franceschini, and A. Massa are with the Department of Information and Communication Technology, University of Trento, Via Sommarive 14 - 38050 Trento - ITALY, Tel.: +39 0461 882057, Fax: +39 0461 882093, E-mail: *andrea.massa@ing.unitn.it*, {*massimo.donelli, davide.franceschini, gabriele.franceschini*}*@dit.unitn.it*, Web-site: *http://www.eledia.ing.unitn.it*

TE scattered data are expected to give different information on the scenario under test [21] and maybe a larger amount since two field components are taken into account. Moreover, as pointed out in [21], the influence of the ill-posedness for TE inverse scattering is lower than that for TM since the Green's function is more singular in the former case. However, the computational load for exploiting such positive features is unavoidably increased because of the need of solving a vectorial problem characterized by a stronger non-linearity [22]. As a matter of fact, by considering the same spatial resolution for reconstructing the unknown profile in the investigation domain, the dimension of the space of unknowns turns out to be larger for TE than for TM case. Thus, retrieval procedures able to effectively deal with large-dimension problems are necessary.
The need of a high resolution accuracy in presence of a limited information content of collectable data [23] has been successfully addressed for TM data by considering multiresolution strategies [24][25][26][27][28][29], which also allows an increasing of the ratio between data and unknowns useful for reducing the occurrence of local minima [30]. Therefore, what this paper accomplishes is to efficiently use a multiresolution strategy [i.e., the Iterative Multi-Scaling Methodology (IMSA)] for TE scattering data and compare the performance to the TM case. This is the first time, to the best of the authors' knowledge, that a multiresolution methodology is applied to TE scattered data.
The paper is organized as follows. After the mathematical formulation of the inverse scattering problem (Sect. 2), Section 3 will focus on the implementation details of the multistep reconstruction algorithm in dealing with a transverse electric polarization. Successively, the advantages of the IMSA-TE will be analyzed and discussed in Sect. 4 through a numerical analysis concerned with the reconstruction of dielectric and metallic profiles from both synthetic and experimental data. Finally, some conclusions and future developments will be outlined (Sect. 5).

II. Mathematical Formulation

Let us consider a set of monochromatic incident electric fields ($\mathbf{E}^v_{inc}(\mathbf{r})$, $v = 1, ..., V$) at a fixed angular frequency ω that illuminates, from V different angles of incidence, an inhomogeneous object located in a bounded investigation domain D_I lying in free-space (Fig. 1). The unknown object is described through the so-called object function $\tau(\mathbf{r})$ given by

$$\tau(\mathbf{r}) = \varepsilon_r(\mathbf{r}) - 1 - j\frac{\sigma(\mathbf{r})}{\omega\varepsilon_o} \tag{1}$$

where $\varepsilon_r(\mathbf{r})$ is the relative permittivity with respect to the background and $\sigma(\mathbf{r})$ is the conductivity of the scatterer. The total electric field $\mathbf{E}^v_{tot}(\mathbf{r})$, $v = 1, ..., V$, inside and outside the scatterer satisfies the following integral equation

$$\mathbf{E}^v_{tot}(\mathbf{r}) = \mathbf{E}^v_{inc}(\mathbf{r}) + k_0^2 \int_{D_I} \tau(\mathbf{r}')\mathbf{E}^v_{tot}(\mathbf{r}') \cdot \underline{\mathbf{G}}(\mathbf{r}|\mathbf{r}')\, d\mathbf{r}' \tag{2}$$

where $k_0^2 = \omega^2\mu_0\varepsilon_0$, $\underline{\mathbf{G}}(\mathbf{r}|\mathbf{r}')$ is the dyadic Green's function and $\mathbf{r}' \in D_I$ identifies a point inside the investigation area, while $\mathbf{r}$ refers to a location of the investigation domain or of the measurement domain D_M external to D_I.
Equation (2) is the basic relationship for developing any inversion algorithm based on the integral equation formulation. Moreover, in the following, a tomographic configuration will be assumed [$\tau(\mathbf{r}) = \tau(x, y)$, z being the axis of symmetry of the scatterer].
For 2D TM polarization, the electric field is parallel to the invariance axis of the cylindrical target, $\mathbf{E}^v_{inc}(x, y) = E^v_{z,inc}(x, y)\hat{\mathbf{z}}$. Thus, equation (2) reduces to a scalar relation

$$\begin{array}{c} E^v_{z,tot}(x, y) = E^v_{z,inc}(x, y) + k_0^2 \int_{D_I} G(x, y|x', y')\tau(x', y') \\ E^v_{z,tot}(x', y')\, dx'dy' \qquad \forall (x, y);\ (x', y') \in D_I \end{array} \tag{3}$$

where $G(x, y|x', y') = -\frac{j}{4}H_0^{(2)}\left(k_0\sqrt{(x - x')^2 + (y - y')^2}\right)$, $H_0^{(2)}$ being the second kind 0*th*-order Hankel function and $j^2 = -1$.
Because of the non linear nature of the problem in hand and its intrinsic ill-posedness, the electromagnetic inversion is performed by looking for a configuration of the unknowns [i.e., $\tau(x, y)$ and $E^v_{z,tot}(x, y)$ in D_I] that minimizes the fitting between retrieved and known field samples.

For 2D TE polarization, the problem in hand turns out to be more complicated since it cannot be described in terms of electric-field formulation through a scalar formulation[(1)1]. In this case, $\mathbf{E}^v_{inc}(x,y) = E^v_{x,inc}(x,y)\hat{\mathbf{x}} + E^v_{y,inc}(x,y)\hat{\mathbf{y}}$.
The domain integral equation for the electric field vectors is given by

$$\mathbf{E}^v_{tot}(\mathbf{r}) = \mathbf{E}^v_{inc}(\mathbf{r}) + (k_0^2 + \nabla\nabla\cdot)\int_{D_I} G(\mathbf{r}|\mathbf{r}')\cdot\tau(\mathbf{r}')\mathbf{E}^v_{tot}(\mathbf{r}')\,d\mathbf{r}'$$

where the spatial differentiation operates on $\mathbf{r}$.
Starting from this vectorial equation, a TE-based inversion procedure is aimed at retrieving the object function $\tau(x,y)$ and simultaneously two components of the electric field [i.e., $E^v_{x,tot}(x,y)$ and $E^v_{y,tot}(x,y)$, $v = 1,...,V$] in D_I.

III. The Multi-Scaling Approach for the TE Problem

Starting from the mathematical description in terms of Data and State equations, the inverse problem is solved by means of the iterative multiscaling procedure. Since the IMSA has been widely described for the TM case [26][27], in the following only the main issues concerned with the TE case will be briefly resumed.
In general, the main motivation for adopting a multiresolution methodology lies in the limited information content of the collectable data [23] that does not allow an arbitrary resolution level for the unknowns in the investigation domain. Especially for the TE case, the optimal representation of the unknown has to be efficiently addressed since such a vectorial problem is characterized by more unknown parameters with respect to the TM scalar one.
As a matter of fact, the IMSA defines a suitable discretization of the unknown distributions according to the available data [31]. At each step (p being the step index) of the multiscaling process, only a limited number of $N_{(p)}$ basis functions is employed for representing the unknowns in the region-of-interest (RoI) where the scatterer is supposed to be located. Iteratively, the same number of basis functions is reallocated in a reduced area defined according to the criteria given in [27]. Therefore, the original investigation domain (i.e., D_I) turns out to be discretized in a non-uniform way since the spatial resolution is step-by-step enhanced only in a limited sub-domain of D_I. Such a zooming strategy limits the total number of unknown coefficients (weighting the $N_{(p)}$ basis functions) allowing a detailed representation of the scenario where necessary.
As far as the retrieval of the profile under investigation is concerned, the values of the TE unknowns, i.e. $\tau\left(x_{n_{(p)}}, y_{n_{(p)}}\right)$, $E^v_{x,tot}\left(x_{n_{(p)}}, y_{n_{(p)}}\right)$, $E^v_{y,tot}\left(x_{n_{(p)}}, y_{n_{(p)}}\right)$, are obtained by minimizing the following cost function

$$\begin{aligned}
&\Phi_{(p)}\left\{\tau\left(x_{n_{(p)}}, y_{n_{(p)}}\right), E^v_{c,tot}\left(x_{n_{(p)}}, y_{n_{(p)}}\right); c = x,y\right.\\
&\left. n_{(p)} = 1,...,N_{(p)} \quad v = 1,...,V\right\} = \Phi^{Data}_{(p)} + \Phi^{State}_{(p)}\\
&\Phi^{Data}_{(p)} = \sum_{c=x,y}\left\{\sum_{v=1}^{V}\sum_{m_{(v)}=1}^{M_{(v)}}\right.\\
&\alpha^{Data}_c\left| E^v_{c,tot}\left(x_{m_{(v)}}, y_{m_{(v)}}\right) - E^v_{c,inc}\left(x_{m_{(v)}}, y_{m_{(v)}}\right)\right.\\
&-\sum_{n_{(p)}=1}^{N_{(p)}}\sum_{d=x,y}\tau\left(x_{n_{(p)}}, y_{n_{(p)}}\right)E^v_{d,tot}\left(x_{n_{(p)}}, y_{n_{(p)}}\right)\\
&\left.\left. G_{cd}\left(x_{m_{(v)}}, y_{m_{(v)}}\middle| x_{n_{(p)}}, y_{n_{(p)}}\right)\right|^2\right\}\\
&\Phi^{State}_{(p)} = \sum_{c=x,y}\left\{\sum_{v=1}^{V}\sum_{n(p)=1}^{N_{(p)}}\beta^{State}_c\left| E^v_{c,inc}\left(x_{n_{(p)}}, y_{n_{(p)}}\right)\right.\right.\\
&-\left[E^v_{c,tot}\left(x_{n_{(p)}}, y_{n_{(p)}}\right) - \sum_{u_{(p)}=1}^{N_{(p)}}\sum_{d=x,y}\tau\left(x_{u_{(p)}}, y_{u_{(p)}}\right)\right.\\
&\left.\left.\left. E^v_{d,tot}\left(x_{u_{(p)}}, y_{u_{(p)}}\right)G_{cd}\left(x_{n_{(p)}}, y_{n_{(p)}}\middle| x_{u_{(p)}}, y_{u_{(p)}}\right)\right]\right|^2
\end{aligned} \tag{4}$$

where

$$\alpha^{Data}_c = \frac{\alpha_c}{\sum_{v=1}^{V}\sum_{m_{(v)}=1}^{M_{(v)}}\left|E^v_{c,tot}\left(x_{m_{(v)}}, y_{m(v)}\right) - E^v_{c,inc}\left(x_{m_{(v)}}, y_{m(v)}\right)\right|^2} \tag{5}$$

and

$$\beta^{State}_c = \frac{\beta_c}{\sum_{v=1}^{V}\sum_{n(p)=1}^{N_{(p)}}\left|E^v_{c,inc}\left(x_{n_{(p)}}, y_{n_{(p)}}\right)\right|^2}. \tag{6}$$

[1] In the TE case, the domain integral equation can be formulated as a scalar-domain integral equation with the one non-zero magnetic-field component as the unknown field or in terms of a vector integral equation with the electric-field vector (two nonzero components) as the unknown field. In [20], it has been shown that the single magnetic-field formulation turns out to be inferior to the dual electric-field formulation.

Moreover, α_c and β_c are weighting coefficients related to the c-th field component; G_{xx}, $G_{xy} = G_{yx}$, and G_{yy} are given by

$$G_{xx}\left(x_h, y_h | x_k, y_k\right) = \begin{cases} -j\frac{\pi a_k J_1(k_o a_k)}{2\rho_{hk}^3}\left[k_o\rho_{hk}y_{hk}^2 H_o^{(2)}\left(k_o\rho_{hk}\right)\right. \\ \left. + \left(x_{hk}^2 - y_{hk}^2\right) H_1^{(2)}\left(k_o\rho_{hk}\right)\right] & h \neq k \\ -\frac{j}{4}\left[\pi k_o a_k H_1^{(2)}\left(k_o a_k\right) - 4j\right] & h = k \end{cases} \tag{7}$$

$$G_{xy}\left(x_h, y_h | x_k, y_k\right) = \begin{cases} -j\frac{\pi a_k J_1(k_o a_k)}{2\rho_{hk}^3} x_{hk}y_{hk}\left[2H_1^{(2)}\left(k_o\rho_{hk}\right)\right. \\ \left. - k_o\rho_{hk}H_o^{(2)}\left(k_o\rho_{hk}\right)\right] & h \neq k \\ 0 & h = k \end{cases} \tag{8}$$

$$G_{yy}\left(x_h, y_h | x_k, y_k\right) = \begin{cases} -j\frac{\pi a_k J_1(k_o a_k)}{2\rho_{hk}^3}\left[k_o\rho_{hk}x_{hk}^2 H_o^{(2)}\left(k_o\rho_{hk}\right)\right. \\ \left. - \left(x_{hk}^2 - y_{hk}^2\right) H_1^{(2)}\left(k_o\rho_{hk}\right)\right] & h \neq k \\ -\frac{j}{4}\left[\pi k_o a_k H_1^{(2)}\left(k_o a_k\right) - 4j\right] & h = k \end{cases} \tag{9}$$

where $\rho_{hk} = \sqrt{x_{hk}^2 + y_{hk}^2}$, $x_{hk} = (x_h - x_k)$ and $y_{hk} = (y_h - y_k)$. Moreover, J_1 is the first order Bessel function and $H_1^{(2)}$ is the second kind Hankel function of first order, respectively; $a_k = \sqrt{\frac{A_k}{\pi}}$, A_k being the area of the *k*-th discretization sub-domain.

The minimization of (4) is iteratively performed with a conjugate-gradient procedure. Even though more efficient optimization techniques are currently under study for the TE case and they have been already developed for the TM case [32], the use of a deterministic technique for this analysis is motivated by the need of focusing on the effectiveness of a "pure" IMSA in dealing with TE date neglecting the "overboost" effects as well as the randomness arising from its integration with a stochastic optimizer (more effective in avoiding the solution is trapped in the local minima of the cost function).

Finally, the multistep procedure terminates at $p = p_{opt}$ when the stability conditions, defined in [27] for the TM case, hold true.

IV. Numerical Analysis

In this section, illustrative reconstructions will be displayed and discussed in order to assess the effectiveness of the IMSA in dealing with TE data. Three different scenarios will be considered: the case of a single dielectric scatterer (Sect. 4.1), the case of multiple dielectric scatterers (Sect. 4.2), and the case of metallic targets in both synthetic and experimental environments (Sect. 4.3). The results will consist of gray-level maps of the object functions, variations of the multiresolution cost function versus the iteration number k, behaviors of some representative error figures versus the signal-to-noise ratio (SNR) characterizing the scattered data, and samples of the cost function along fixed directions in the solution space.

A. Single Dielectric Scatterer

The first example deals with a homogeneous square dielectric profile ($\tau_0 = 0.5$) of side $L_0 = 0.48\lambda_0$, positioned at $x_0 = -0.24\lambda_0$, $y_0 = 0.48\lambda_0$ [Fig. 2(*a*)]. A square investigation domain $L_{D_I} = 2.4\lambda_0$ in side has been assumed and it has been partitioned in $N_{(p)} = 36$ cells. The reconstruction has been carried out exploiting multiview data collected from $V = 4$ different directions of illumination by means of $M_{(v)} = 21$ receivers located on a circular observation curve of radius $1.8\lambda_0$. The maps of the retrieved profiles during the multistep reconstruction process are reported in Figs. 2(*b*)-2(*e*). As it can be observed, the retrieved object function evolves from a low-resolution representation [$\tilde{\tau}_{(1)}$ - Fig. 2(*b*)] to the convergence profile [$\tilde{\tau}_{(p_{opt})}$ - Fig. 2(*e*) and Fig. 3(*c*)-(*d*)], achieved after $p_{opt} = 4$ steps and characterized by the lowest values of the error figures given in Tab. I and computed as follows

$$\delta^{(s)} = \frac{\sqrt{\left[\tilde{x}_0^{(s)} - x_0^{(s)}\right]^2 + \left[\tilde{y}_0^{(s)} - y_0^{(s)}\right]^2}}{\lambda_0}, \quad s = 1, ..., S \tag{10}$$

$$\Delta^{(s)} = \left\{ \frac{\left| \tilde{L}_0^{(s)} - L_0^{(s)} \right|}{L_0^{(s)}} \right\} \times 100, \qquad s = 1, ..., S \tag{11}$$

$$\xi_{(i)}^{(s)} = \sum_{p=1}^{p_{opt}} \frac{1}{N_{(p)}^{(j)}} \sum_{n_{(p)}=1}^{N_{(p)}^{(j)}} \left\{ \left| \frac{\tilde{\tau}^{(s)}\left(x_{n_{(p)}}, y_{n_{(p)}}\right) - \tau_0^{(s)}\left(x_{n_{(p)}}, y_{n_{(p)}}\right)}{\tau_0^{(s)}\left(x_{n_{(p)}}, y_{n_{(p)}}\right)} \right| \right\} \times 100 \tag{12}$$

where j ranges over the whole investigation domain ($j = int$), over the area occupied by the actual scatterers ($j = int$) or over the background ($j = ext$) and the index s indicates the s-th object lying in the investigation domain.

Focusing on such a convergence profile, the numerical values of Tab. I confirm the effectiveness of the inversion algorithm in exploiting TE data for reconstructing the shape of the object ($\delta_{TE} = 2.0 \times 10^{-4}$, $\Delta_{TE} = 12.33$) as well as its dielectric properties ($\xi_{tot}^{TE} = 0.21$).

In order to better appreciate the reconstruction accuracy achieved by the IMSA applied to TE data (even though in noiseless conditions), the same profile has been retrieved using TM data. Since the TE illumination provides two components of the field (E_x^v, E_y^v) and more information it is expected to be collected on the sensed scenario, an overall imaging enhancement compared to the reconstruction obtained with a TM illumination should be verified. In order to check such a supposition, the result of the IMSA-TM inversion is shown in Fig. 3(*a*)-(*b*). As expected, despite the reconstruction is satisfactory, the estimated error figures (Tab. I) are higher than those of the TE experiment. In particular, although for a noiseless experiment, the localization accuracy is decreased ($\frac{\delta^{TM}}{\delta^{TE}} \simeq 20$) and the overall estimation of the dielectric distribution worse as indicated by the values of the quantitative error figures: $\frac{\xi_{ext}^{TM}}{\xi_{ext}^{TE}} \simeq 21.5$, $\frac{\xi_{int}^{TM}}{\xi_{int}^{TE}} \simeq 1.4$, and $\frac{\xi_{tot}^{TM}}{\xi_{tot}^{TE}} \simeq 1.5$.

As far as the trade-off between enhancement of the reconstruction accuracy and increasing of the computational costs in dealing with a TE illumination is concerned, Fig. 4 gives some indications on the minimization of the multiresolution cost function $\Phi_{(p)}$ at the different steps of the IMSA. The spikes occur when the investigation area is scaled and the supports of the basis functions are redefined. In such points, the minimization of the functional starts with an higher level of resolution. For a comparative analysis, the behavior of the cost function for the TM case in shown, as well. As can be noticed, on the one hand, the TE cost function reaches a lower value and a more accurate fitting with the problem data, thus justifying a better reconstruction. On the other hand, the processing of the TE scattering data requires an additional amount of computational resources (Tab. II) in terms of both total number of iterations $K_{opt}^{TE} \simeq 4.5 K_{opt}^{TM}$ ($K_{opt} = \sum_{p=1}^{p_{opt}} k_{(p)}^{conv}$, $k_{(p)}^{conv}$ being the number of iterations needed to achieve "convergence" at the pth step of the multiscaling process) and mean time per iteration ($t_{iter}^{TE} = 120\ ms$ versus $t_{iter}^{TM} = 36\ ms$). Such an increment is related to the presence of two components of the fields that contribute at enlarging the amount of independent achievable data as well as the number of unknowns, which causes a larger memory allocation $U^{TE} = 3U^{TM}$ and processing load.

Because of the increased dimension of the solution space and of the use of a deterministic procedure, it is convenient to analyze the "shape" of the IMSA cost function as well as the occurrence of local minima in such a functional. As a matter of fact, the inversion process is performed minimizing (4), thus the complexity as well as the reliability of the reconstruction is strongly related to the presence of local minima that represent false solutions of the problem in hand. For illustrative purposes, Figs. 5(*a*)-(*b*) show the plots of the values of the cost function computed in correspondence with an object with the same support of the actual scatterer and varying the value of the object function in the range $0.0 \leq \tilde{\tau} \leq 16.0$. By so doing, a particular direction of the solution space is explored and some indications about the shape of $\Phi_{(p)}$ can be inferred. First of all, let us observe that, as expected, the global minimum of the cost function turns out to be at $\tilde{\tau} = \tau_0 = 0.5$.

As can be noticed, the comparison between TE and TM (concerned with $V = 1$) points out that the number of local minima for the TE case [Fig. 5(*a*)] is slightly inferior than for the TM case [Fig. 5(*b*)]. Moreover, even though the number of views is increased ($V \geq 2$), other minimum points in addition to the global one occur in the TM case [Fig. 5(*b*)], while no local

minima can be observed along this "direction" of the solution space under TE illumination [Fig. 5(*a*)].

Therefore, although such an example cannot be considered as a definitive indication on the number and on the occurrence of the local minima (since it considers only a sampling direction in the solution space), it seems to confirm also for the TE illumination a key-feature of the IMSA, that is the "reduction" of local minima and, in the first resort/approximation, a certain reason of using a deterministic method as minimizer.

Finally, since the TE exploits the information from two independent field polarizations (E_x^v - TE_x, E_y^v - TE_y) and it outperforms the TM inversion of dielectric profiles, which considers only a scalar field component (E_z^v - TM), it could be interesting to assess the effectiveness of the IMSA procedure when each TE scalar component is individually processed. Towards this end, the inversion process has been carried out by assuming $\alpha_x = \beta_x = 1.0$ and $\alpha_y = \beta_y = 0.0$ (TE_x illumination) and $\alpha_x = \beta_x = 0.0$ and $\alpha_y = \beta_y = 1.0$ (TE_y illumination) in the cost function (4). The grey-level maps of the retrieved profiles are shown in Fig. 3(*e*) and Fig. 3(*f*), respectively. The obtained results highlight that only the simultaneous processing of both the TE components is needed for obtaining a more faithful reconstruction than the TM inversion. Moreover, it seems to further confirm that TM and TE illuminations give unrelated data about the scatterer [21] (as a matter of fact different reconstructions have been obtained with the two different datasets), but also that each TE component supplies a different information on the scenario under test.

B. Multiple Dielectric Scatterers

The second example of the numerical validation considers a more complex scenario where a multiple scatterers configuration lies. Let us refer to the reference geometry shown in Fig. 6 where three equal square cylinders ($L_0^{(s)} = 0.67\lambda_0$, $s = 1, ..., 3$, in side) located at ($x_0^{(1)} = y_0^{(1)} = 0.67\lambda_0$), ($x_0^{(2)} = -y_0^{(2)} = -0.67\lambda_0$), and ($x_0^{(3)} = 0$, $y_0^{(3)} = -0.67\lambda_0$) are embedded in a search area $L_{D_I} = 4\lambda_0$-sided. The value of the object function in the region occupied by the scatterers is equal to $\tau_0^{(s)} = 0.5$, $s = 1, ..., 3$. The objects have been probed from $V = 8$ directions and the scattered fields have been collected at $M_{(v)} = 35$, $v = 1, ..., V$ positions. Moreover, at the first step ($p = 1$) of the multiscaling process, the investigation domain has been partitioned in $N_{(1)} = 100$ subdomains. For comparison purposes, the reconstruction has been carried out with both TE and TM illuminations. Moreover, for a more exhaustive assessment also noisy data have been taken into account. Towards this end, the scattered field values have been blurred as in [26] by adding a gaussian contribution with a zero mean value and identified by a fixed SNR value.

Figure 7 shows in a comparative fashion the achieved results. Pictorially, one can notice a better estimation of the supports of the scatterers when a TE illumination is used. Such an indication is quantitatively confirmed by the values of the error index Δ reported in Tab. III and IV. More in detail, when $SNR \leq 10\ dB$, $11.42 \leqslant \Delta_{TE}^{(s)} \leqslant 16.44$ for the TE case, while its range of variations turns out to be higher in correspondence with TM reconstructions ($15.80 \leqslant \Delta_{TM}^{(s)} \leqslant 25.82$). As far as the quantitative imaging is concerned, the total error ξ_{tot}^{TE} is lower than 2.6 in the TE configuration whatever the SNR value, while $\xi_{tot}^{TM}\big|_{SNR=10\,dB} \simeq 3$ and $\xi_{tot}^{TM}\big|_{SNR=5\,dB} \simeq 4.2$. Moreover, the values of $\xi_{int}^{(s)}$ clearly indicate a more accurate retrieval of the object function in the regions occupied by the scatterers.

For completeness, Tab. V provides some details of the computational burden of the iterative reconstruction processes. When the noise level is negligible, the same conclusions drawn for the single scatterer scenarios hold true and the $IMSA-TM$ turns out to be more effective in reaching the convergence. On the other hand, the convergence rates are quite similar for lower SNRs. However, the $IMSA-TE$ seems to converge faster in strong noise conditions (5dB) and to enhance the accuracy ($\frac{\xi_{tot}^{TM}\big|_{SNR=5\,dB}}{\xi_{tot}^{TE}\big|_{SNR=5\,dB}} \simeq 1.7$). This points out the positive effect of the exploitation of the two field components especially in critical measurement conditions.

To further assess the proposed approach with multiple scatterers and noisy conditions, also evaluating the "discrimination" capabilities of the method, a third experiment concerned with a two-objects configuration [Fig. 8(*a*) - $\tau_0^{(s)} = 0.5$, $s = 1, 2$] has been carried out. The scatterers differ in dimensions, $L_0^{(1)} = 1.33\lambda_0$ and $L_0^{(2)} = 0.67\lambda_0$, while the illumination/measurement setup is the same of the previous example.

In order to give a complete overview of the obtained results, Fig. 9 shows the behaviors of the error indexes versus the SNR. In general, whatever the noise level, the $IMSA-TE$ yields better inversions both in locating [Fig. 9(*a*)] and shaping [Fig. 9(*b*)] the scatterers, as well as in quantitatively estimating their dielectric profiles [Fig. 9(*c*)]. In particular, the TE-based

approach significantly overcomes the TM-based technique when the noise level grows (i.e., $SNR < 15\ dB$). In such a situation, the inversion turns out to be more difficult and the $IMSA$ benefits of the enhanced amount of information. Such an improvement can be also pictorially appreciated in Fig. 8 where the grey-levels maps of the dielectric profiles retrieved when $SNR = 5\ dB$ under TE illumination [Fig. 8(*b*)] and TM illumination [Fig. 8(*c*)] are reported, respectively. In particular, for such a configuration, the details of the error figures are reported in Tab. VI.

As far as the computational burden is concerned, the same conclusions of the previous example can be inferred also for this test case (Tab. VII).

C. Metallic Targets

Finally, the last set of experiments is aimed at evaluating the reconstruction of metallic targets both considering synthetic and real data. Figure 10(*a*) shows the reference distribution of the metallic ($\sigma = 20\ S/m$) object under test of side $L_0 = 0.48\lambda_0$ and centered at $x_0 = -0.24\lambda_0$, $y_0 = 0.48\lambda_0$. As far as the configuration of the experimental setup is concerned, the following parameters have been used: $L_{D_I} = 1.6\lambda_0$, $V = 4$, and $M_{(v)} = 36$. Moreover, D_I has been partitioned in $N_{(1)} = 21$ subdomains. The reconstruction results give different indications on the effectiveness of $IMSA - TE$ vs. $IMSA - TM$ in comparison with those carried out for the dielectric configurations (Sect. 4.1 and Sect. 4.2). As a matter of fact, the profile under test is generally better imaged when a TM illumination is considered as pointed out by the maps in Figs. 10(*b*)-(*c*) ($SNR = 10\ dB$). Quantitatively, $\xi_{tot}^{TE} = 7.16$ vs. $\xi_{tot}^{TM} = 3.86$, $\xi_{int}^{TE} = 41.72$ vs. $\xi_{int}^{TM} = 27.73$, and $\Delta^{TE} = 2.2\Delta^{TM}$.

However, such a behavior is not surprising since the same difficulties in dealing with a TE illumination of impenetrable obstacles have been encountered also by *Ramananjaona et al.* [33] both using synthetic and real data.

To further analyze such an issue, also laboratory-controlled data concerned with the experimental dataset "Marseille" [34] have been used. In particular, for a comparative study, the scattered data related to a rectangular metallic target ($25.4 \times 12.7\ mm^2$) probed with a TM ("*rectTM_cent.exp*") and a TE ("*rectTE_8f.exp*") incident field have been considered. Because of the limited aspect of the measurement, the whole set of data ($V = 36$, $M_{(v)} = 49$) at $f = 4\ GHz$ has been precessed imposing a constraint on the real part of object function [$Re\,(\tilde{\tau}) = 0$] and performing a thresholding (as suggested in [35]) to $\Upsilon_{max} = -10.5$ if $Im\,\{\tau(x,y)\} > \Upsilon_{max}$.

The reconstruction exploiting TM scattered data [Fig. 11(*b*)] is more accurate. The boundaries of the object are better detected and the metallic nature of the scatterer is more faithful estimated. Similar observations have been also made in [33] and [36] where different inversion methods were used. For a preliminary comparison between IMSA-TE and another inversion approach, Fig. 11(*c*) reports the reconstructed profile obtained with the CSI-TE algorithm [36]. The inversion of the experimental data has been carried out considering single frequency measurements ($f = 4\ GHz$) for reconstructing an investigation region $17\,cm$ in side. Such single-step strategy achieves a reconstruction in which the dimension of the profile is slightly underestimated, as well as the retrieved value of the imaginary part is greater than $Im\,\{\tau(x,y)\}_{CSI-TE}^{min} = -0.6$ (while $Im\,\{\tau(x,y)\}_{IMSA-TE}^{min} = -3.1$). However, for further comparisons with CSI and other different kinds of inversion algorithms the reader may refer to the papers in [34].

The worse reconstructions with TE data could be related to the measurement setup. As a matter of fact, for the TE case only one electric field component (i.e., perpendicular to the radial direction) has been measured instead of two orthogonal in the azimuthal plane as required by the vectorial nature of the problem inside D_I. Such supposition agrees with other works in literature on the same dataset, but should be further verified other impenetrable objects or experiments in which the electric field is completely measured.

Moreover, problems are expected with the metallic or high contrast objects when the TE problem is formulated in term of the electric field. As a matter of fact, it is the electric flux rather that the electric field that is continuous in an inhomogeneous medium, right at the boundary of an object. Unfortunately, enforcing this physics in the IMSA would make the gradient quite nonlinear and involved.

V. Conclusion

An iterative multiresolution method for the reconstruction of unknown scatterers illuminated by TE incident fields has been presented. Such a multiscaling algorithm provides a multistep reconstruction of the scenario under test focusing on some RoIs

adaptively determined by means of the information acquired during the iterative minimization of a suitable multiresolution cost function.

The numerical analysis carried out through the paper has shown that the proposed methodology presents very attractive capabilities in imaging single and multiple scatterers and a better reconstruction accuracy compared to the TM illumination when dielectric scatterers are dealt with. An opposite conclusion has been carried out when metallic scatterers are probed both considering synthetic and real data. This behavior, even though a more exhaustive analysis would be necessary, suggests the need of extending the $IMSA$ procedure to a hybrid strategy where TM and TE illuminations (when available) are alternatively processed as proposed in [21].

Moreover, the IMSA-TE has been compared with a single-step CSI-TE inversion algorithm. The multiresolution reconstruction has given better results in estimating the metallic characteristics of the scatterer, however a wider analysis should be carried out in order to fully asses the comparative analysis between the two methodologies. Certainly, it would be interesting to develop a multiscaling procedure based on the contrast source formulation.

Finally, it should be pointed out that the proposed solution of the TE case is an intermediate and mandatory step towards the solution of the full three-dimensional problem where all the three scalar components of the electric field play their role. The main differences for such an extension lie in the computation time (expected to substantially increase) as well as in the minimization procedure to be carefully implemented in order to suitably deal with the larger solution space.

ACKNOWLEDGMENT

The authors wish to thank Dr. A. Abubakar for kindly providing the experimental results of the CSI algorithm.

REFERENCES

[1] J. C. Bolomey and C. Pichot, “Microwave tomography: from theory to practical imaging systems,” *Int. J. Imag. Sys. Tech.*, vol. 2, pp. 144-156, 1990.

[2] J. C. Bolomey, “Recent European developments in active microwave imaging for industrial, scientific, and medical applications,” *IEEE Trans. Microwave Theory Tech.*, vol. 37, pp. 2109-2117, Jun. 1989.

[3] J. Ch. Bolomey, “Microwave imaging techniques for NDT and NDE,” *Proc. Training Workshop on Advanced Microwave NDT/NDE Techniques*, Supelec/CNRS, Paris, Sep. 7-9, 1999.

[4] A. Massa and S. Caorsi, Special Issue on “Microwave imaging and inverse scattering techniques,” *J. Electromagn. Waves Applicat*., vol. 17, Apr. 2003.

[5] R. M. Lewis, “Physical optics inverse diffraction,” *IEEE Trans. Antennas Propagat.*, vol. 17, pp. 308-314, May 1969.

[6] T. H. Chu and N. H. Farhat, “Polarization effects in microwave diversity imaging of perfectly conducting cylinders,” *IEEE Trans. Antennas Propagat*., vol. 37, pp. 235-244, Feb. 1989.

[7] J. B. Keller, “Accuracy and validity of Born and Rytov approximations,” *J. Opt. Soc. Am*., vol. 6, pp. 1003-1004, 1969.

[8] M. Stanley, A. C. Kak, and L. E. Larsen, “Limitations of imaging with first-order diffraction tomography,” *IEEE Trans. Microwave Theory Tech.*, vol. 32, pp. 860-874, Aug. 1984.

[9] T. Isernia, V. Pascazio, and R. Pierri, “A nonlinear estimation method in tomographic imaging,” *IEEE Trans. Geosci. Remote Sensing*, vol. 35, pp. 910-923, Jul. 1997.

[10] M. Lambert, D. Lesselier, and B. J. Kooij, “The retrieval of a buried cylindrical obstacle by a constrained modified gradient method in the H-polarization case and for Maxwellian materials,” *Inverse Problems*, vol. 14, pp. 1265-1283, 1998.

[11] A. Massa, *Genetic algorithm based techniques for 2D microwave inverse scattering*. In Recent Research Developments in Microwave Theory and Techniques, Ed. S. G. Pandalai, Transworld Research Network Press, Trivandrum, India, 2002.

[12] W. C. Chew and G. P. Otto, “Microwave imaging of multiple conducting cylinders using local shape functions,” *IEEE Microwave Guided Wave Lett.*, vol. 2, pp. 284-286, Jul. 1992.

[13] K. Belkebir, R. E. Kleinmann, and C. Pichot, “Microwave imaging - Location and shape reconstruction from multifrequency scattering data,” *IEEE Trans. Microwave Theory Tech.*, vol. 45, pp. 469-476, Apr. 1997.

[14] S. Caorsi, A. Massa, and M. Pastorino, "A computational technique based on a real-coded genetic algorithm for microwave imaging purposes," *IEEE Trans. Geoscic Remote Sensing*, vol. 38, pp. 1697-1708, Jul. 2000.

[15] N. Joachimowicz, C. Pichot, and J.-P. Hugonin, “Inverse scattering: An iterative numerical method for electromagnetic imaging,” *IEEE Trans. Antennas Propaga*t., vol. 39, pp. 1742-1752, Dec. 1991.

[16] A. Abubakar, P. M. van den Berg, and J. J. Mallorqui, “Imaging of biomedical data using a multiplicative regularized contrast source inversion method,” *IEEE Trans. Microwave Theory Tech.*, vol. 50, pp. 1761-1771, Jul. 2002.

[17] A. Abubakar and P. M. van den Berg, “Three-dimensional nonlinear inversion in crosswell electrode logging,” *Radio Sci.*, vol. 4, pp. 989-1004, 1998.

[18] F. Li, Q. H. Liu, and L.-P. Song, “Three dimensional reconstruction of objects buried in layered media using Born and distorted Born iterative methods,” *IEEE Trans. Geosci. Remote Sensing*, vol. 1, pp. 107-111, Apr. 2004.

[19] G. Franceschini, D. Franceschini, and A. Massa, “Full-Vectorial Three Dimensional Microwave Imaging trough an Iterative Multi-Scaling Strategy - A preliminary Assessment,” *IEEE Geosci. Remote Sensing Lett.*, vol. 2, pp. 428-432, Oct. 2005.

[20] B. J. Kooij and P. M. van den Berg, "Nonlinear Inversion in TE Scattering," *IEEE Trans. Microwave Theory Tech.*, vol. 46, pp. 1704-1711, Nov. 1998.
[21] C.-P. Chou and Y.-W. Kiang, "Inverse Scattering of Dielectric Cylinders by a cascade TE-TM method," *IEEE Trans. Microwave Theory Tech.*, vol. 47, pp. 1923-1930, Oct. 1999.
[22] J. Ma, W. C. Chew, C.-C. Lu, and J. Song, "Image reconstruction from TE scattering data using equation of strong permittivity fluctuation," *IEEE Trans. Antennas Propagat.*, vol. 48, pp. 860-867, Jun. 2000.
[23] O. M. Bucci and G. Franceschetti, "On the degrees of freedom of scattered fields," *IEEE Trans. Antennas Propagat.*, vol. 37, pp. 918-926, Jul. 1989.
[24] E. L. Miller and A. S. Willsky, "A multiscale, statistically based inversion scheme for linearized inverse scattering problems," *IEEE Trans. Geosci. Remote Sensing*, vol. 34, pp. 346-357, Mar. 1996.
[25] O. M. Bucci, L. Crocco, T. Isernia, and V. Pascazio, "Wavelets in non-linear inverse scattering," *Proc. Geoscience Remote Sensing Symp.*, IGARSS-2000, vol. 7, pp. 3130-3132.
[26] S. Caorsi, M. Donelli, D. Franceschini, and A. Massa, "A new methodology based on an iterative multiscaling for microwave imaging," *IEEE Trans. Microwave Theory Tech.*, vol. 51, pp. 1162-1173, Apr. 2003.
[27] S. Caorsi, M. Donelli, and A. Massa, "Detection, location, and imaging of multiple scatterers by means of the iterative multiscaling method," *IEEE Trans. Microwave Theory Tech.*, vol. 52, pp. 1217-1228, Apr. 2004.
[28] A. Baussard, E. L. Miller, and D. Lesselier, "Adaptive multiscale approach for 2D microwave tomography," *URSI - International Symposium on Electromagnetic Theory*, Pisa, Italia, pp. 1092-1094, May 2004.
[29] A. Baussard, E. L. Miller, and D. Lesselier, "Adaptive multiscale reconstruction of buried objects," *Inverse Problems*, Special section on "Electromagnetic characterization of buried obstacles", W.C. Chew and D. Lesselier eds., vol. 20, pp. S1-S15, 2004.
[30] T. Isernia, V. Pascazio, and R. Pierri, "On the local minima in a tomographic imaging technique," *IEEE Trans. Geosci. Remote Sensing*, vol. 39, pp. 1596-1607, Jul. 2001.
[31] O. M. Bucci and T. Isernia, "Electromagnetic inverse scattering : Retrievable information and measurement strategies," *Radio Sci.*, vol. 32, pp. 2123-2137, 1997.
[32] M. Donelli, and A. Massa, "A computational approach based on a particle swarm optimizer for microwave imaging of two-dimensional dielectric scatterers," *IEEE Trans. Microwave Theory Tech.*, vol. 53, no. 5, pp. 1761-1776, May 2004.
[33] C. Ramananjaona, M. Lambert and D. Lesselier, "Shape inversion from TM and TE real data by controlled evolution of level sets," *Inverse Problems*, vol. 17, pp. 1585-1595, 2001.
[34] K. Belkebir and M. Saillard, Special section: "Testing Inversion Algorithms against Experimental Data," *Inverse Problems*, vol. 17, pp. 1565-1702, Dec. 2001.
[35] P. M. Van den Berg, M. G. Coté, and R. E. Kleinmann, ""Blind" shape reconstruction from experimental data," *IEEE Trans. Antennas Propagat.*, vol. 43, pp. 1389-1396, Dec. 1995.
[36] R. F. Bloemenkamp, A. Abubakar, and P. M. Van den Berg, "Inversion of experimental multi-frequency data using the contrast source inversion method, *Inverse Problem*s, vol. 17, pp. 1611-1622, Dec. 2001.

FIGURE CAPTION

- **Figure 1.** Problem Geometry.
- **Figure 2.** Reconstruction of an off-centered square dielectric cylinder ($\tau_0 = 0.5$) under TE illumination (Noiseless Conditions). Actual profile (*a*) and reconstructed profile at: (*b*) $p = 1$, (*c*) $p = 2$, (*d*) $p = 3$, and (*e*) $p = P_{opt} = 4$.
- **Figure 3.** Reconstruction of an off-centered square dielectric cylinder ($\tau_0 = 0.5$ - Noiseless Conditions). Results obtained (*a*),(*b*) under TM illumination, (*c*),(*d*) under TE illumination, (*e*) exploiting the TE_x component, and (*f*) the TE_y component.
- **Figure 4.** Reconstruction of an off-centered square dielectric cylinder ($\tau_0 = 0.5$ - Noiseless Conditions). Behavior of the multiresolution cost function at the different steps of the minimization procedure for the TE and TM cases.
- **Figure 5.** Reconstruction of an off-centered square dielectric cylinder ($\tau_0 = 0.5$ - Noiseless Conditions). Behavior of the cost function $\Phi_{(p)}$ along a direction of the solution space obtained varying the object function in the range $0 < \tau < 16$: (*a*) TE case and (*b*) and TM case.
- **Figure 6.** Reconstruction of three square dielectric scatterers ($\tau_0^{(s)} = 0.5$, $s = 1, ..., 3$). Actual profile.
- **Figure 7.** Reconstruction of three square dielectric scatterers ($\tau_0^{(s)} = 0.5$, $s = 1, ..., 3$). Retrieved profiles under TE illumination (*a*)(*c*)(*e*) and TM illumination (*b*)(*d*)(*f*) in (*a*)(*b*) noiseless condition, when (*c*)(*d*) $SNR = 10\,dB$, and (*e*)(*f*) when $SNR = 5\,dB$.
- **Figure 8.** Multiple scatterers configuration ($SNR = 5\,dB$). Actual profile (*a*) and reconstructions achieved under TE illumination (*b*) and TM illumination (*c*).
- **Figure 9.** Multiple scatterers configuration. Reconstruction errors versus SNR: (*a*) location errors $\delta^{(s)}$, (*b*) dimensional errors $\Delta^{(s)}$, (*c*) internal errors $\xi_{int}^{(s)}$, and (*d*) external errors $\xi_{ext}^{(s)}$ ($s = 1, 2$).

- **Figure 10.** Reconstruction of an off-centered square metallic cylinder ($\tau_0 = j89.73$). Map of the imaginary part of the reference object function (*a*). Reconstruction of the imaginary part of the object function under (*b*) TE illumination and (*c*) TM illumination ($SNR = 10\ dB$) .
- **Figure 11.** Experimental validation against the real data (Dataset "Marseille" [34]). Reconstruction of the rectangular metallic cylinder at the frequency $f = 4GHz$ when probed with (*a*) a TE incident field ("*rectTE_8f.exp*") and (*b*) a TM incident field ("*rectTM_cent.exp*"). (*c*) Result obtained with the single-step CSI-TE algorithm.

TABLE CAPTION

- **Table I.** Reconstruction of an off-centered Square Dielectric Cylinder ($\tau(x, y) = 0.5 + j0.0$). Comparison of the error figures for the TM and the TE illumination.
- **Table II.** Reconstruction of an off-centered Square Dielectric Cylinder ($\tau(x, y) = 0.5 + j0.0$). Computational Burden.
- **Table III.** Three scatterer configuration. Error figures for the TE illumination.
- **Table IV.** Three scatterer configuration. Error figures for the TM illumination.
- **Table V.** Three scatterer configuration. Convergence step and total iterations number under TE illumination and TM illumination.
- **Table VI.** Multiple Scatterer configuration. Error figures for the TE and TM illumination ($SNR = 5dB$).
- **Table VII.** Multiple Scatterer configuration. Convergence step and total iterations number in the TE case and in the TM illumination.

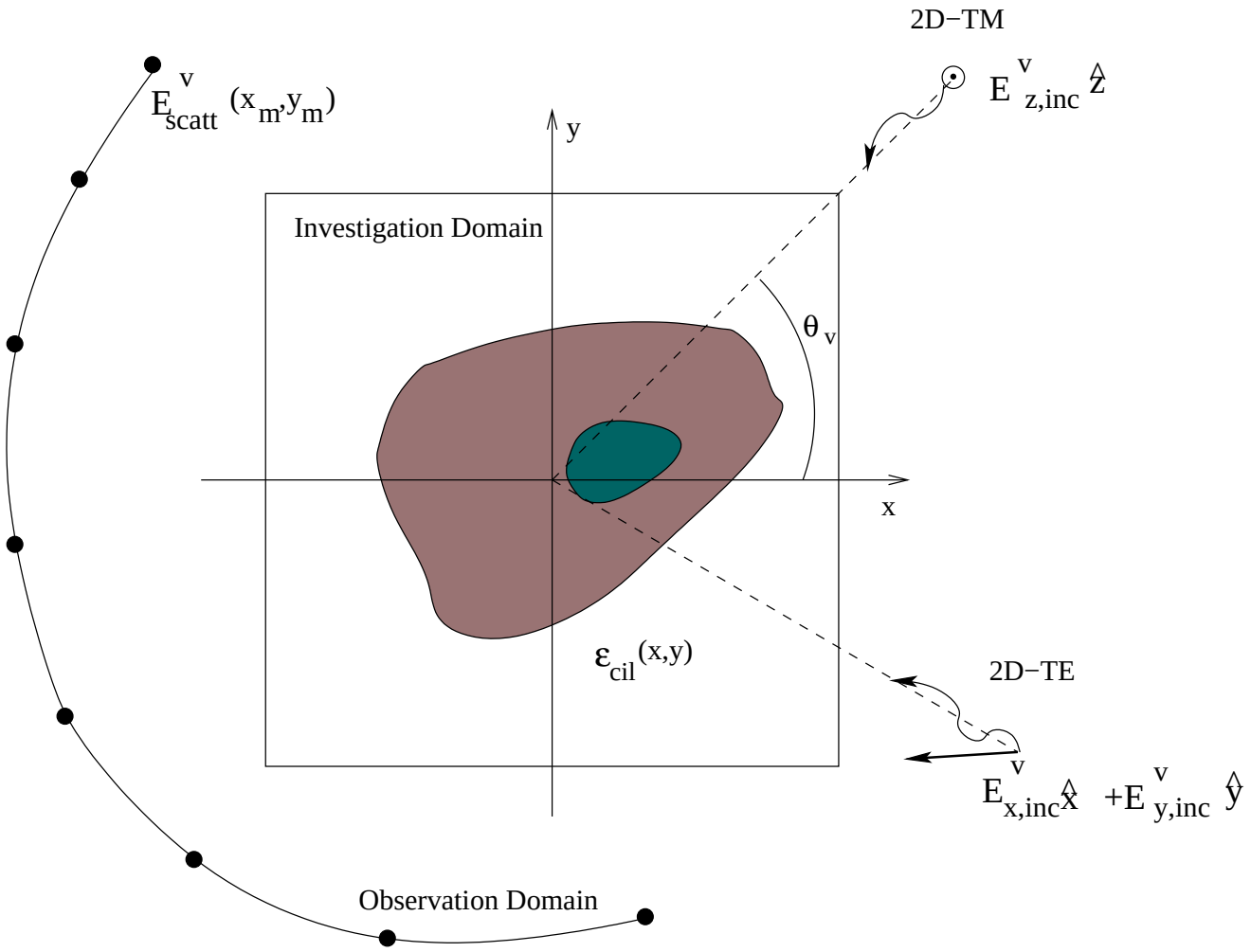

Figure 1 - D. Franceschini *et al., "Iterative Image Reconstruction of ..."*

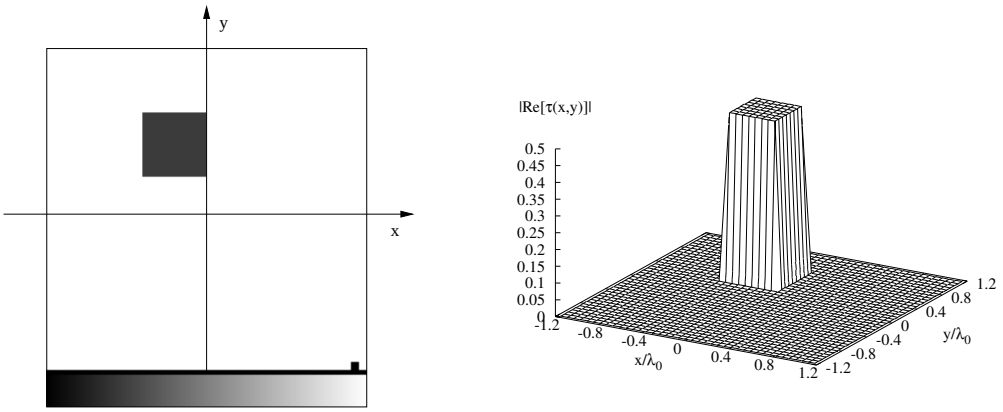

$0.65 \quad Re\{\tau(x,y)\} \quad 0.0$

(*a*)

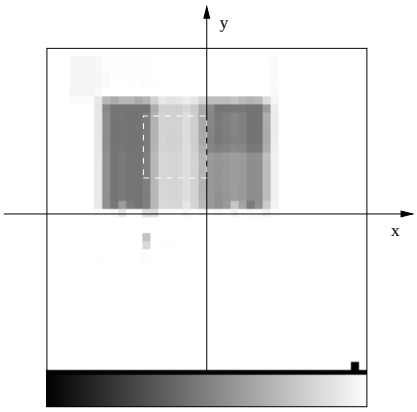

$0.65 \quad Re\{\tau(x,y)\} \quad 0.0$

(*b*)

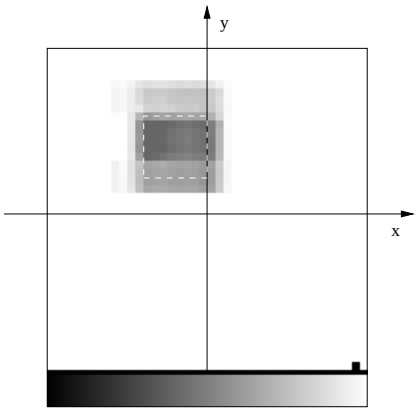

$0.65 \quad Re\{\tau(x,y)\} \quad 0.0$

(*c*)

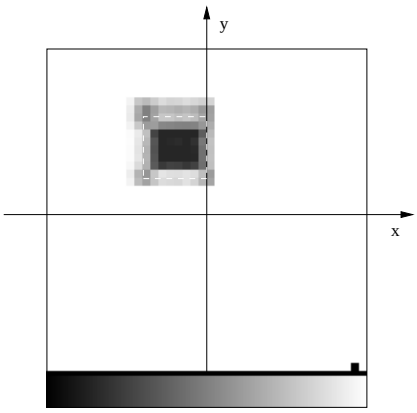

$0.65 \quad Re\{\tau(x,y)\} \quad 0.0$

(*d*)

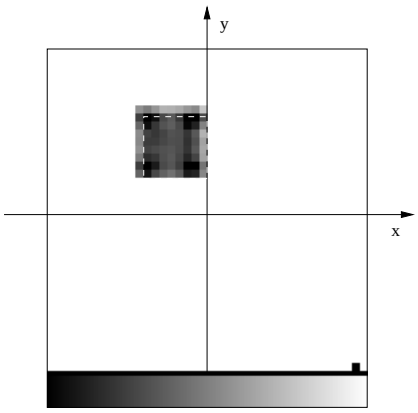

$0.65 \quad Re\{\tau(x,y)\} \quad 0.0$

(*e*)

Figure 2 - D. Franceschini *et al., "Iterative Image Reconstruction of ..."*

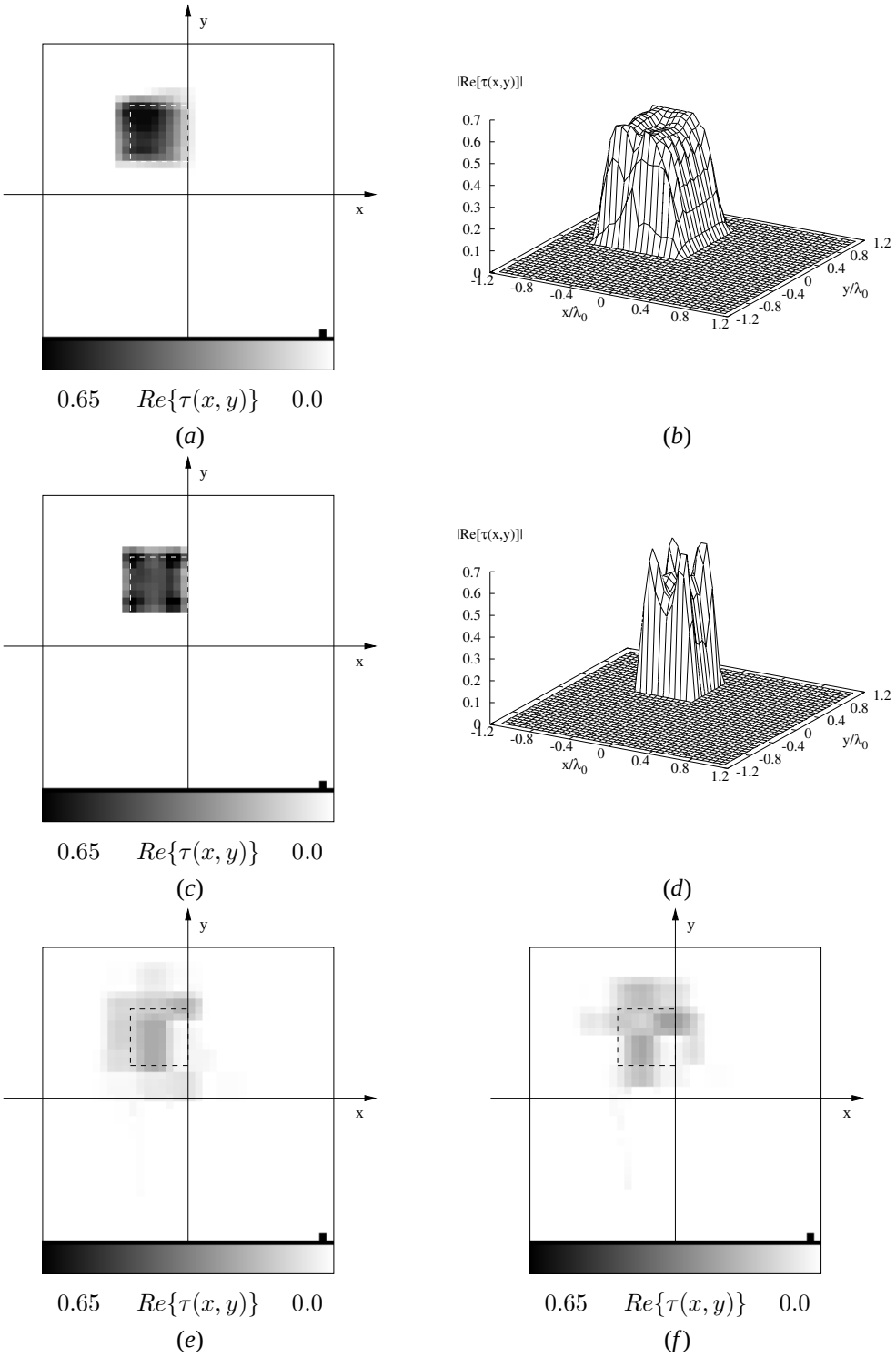

Figure 3 - D. Franceschini *et al., "Iterative Image Reconstruction of ..."*

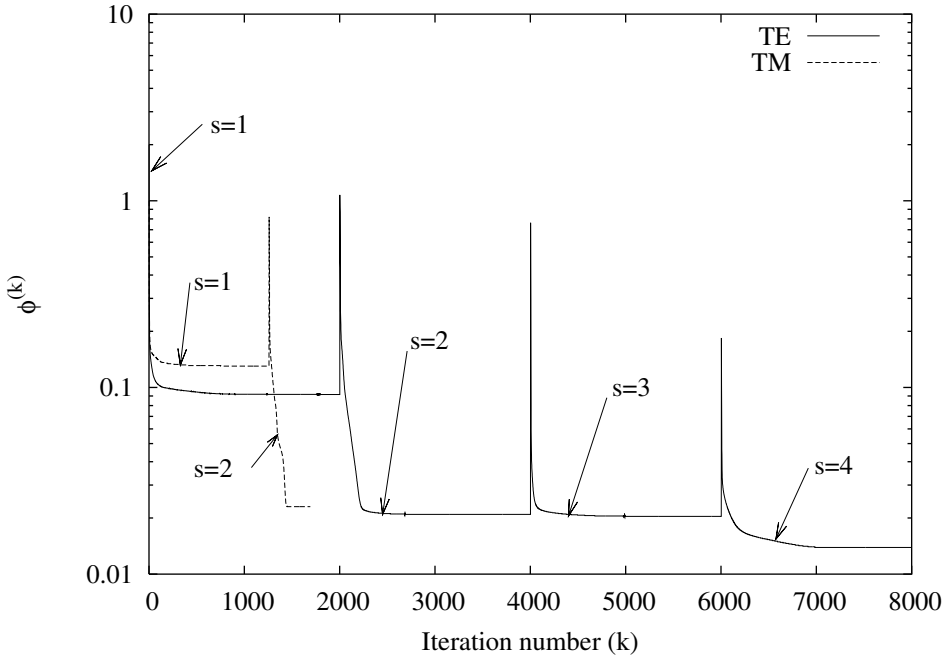

Figure 4 - D. Franceschini *et al.*, "*Iterative Image Reconstruction of ...*"

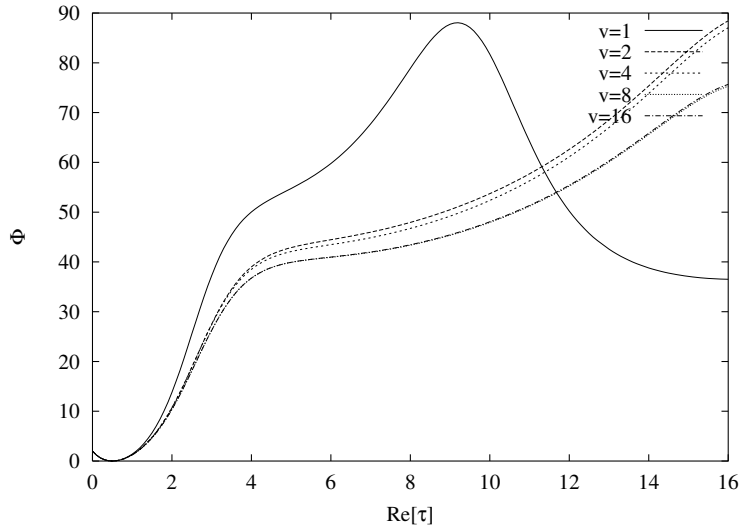

(*a*)

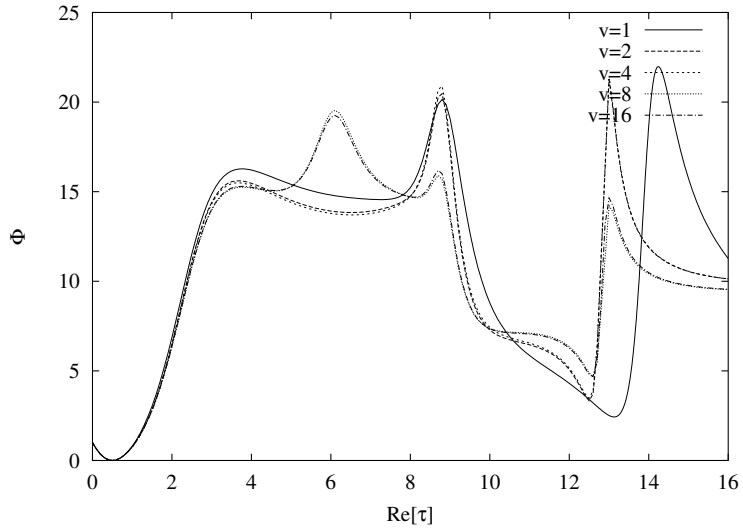

(*b*)

Figure 5 - D. Franceschini *et al.*, "*Iterative Image Reconstruction of ...*"

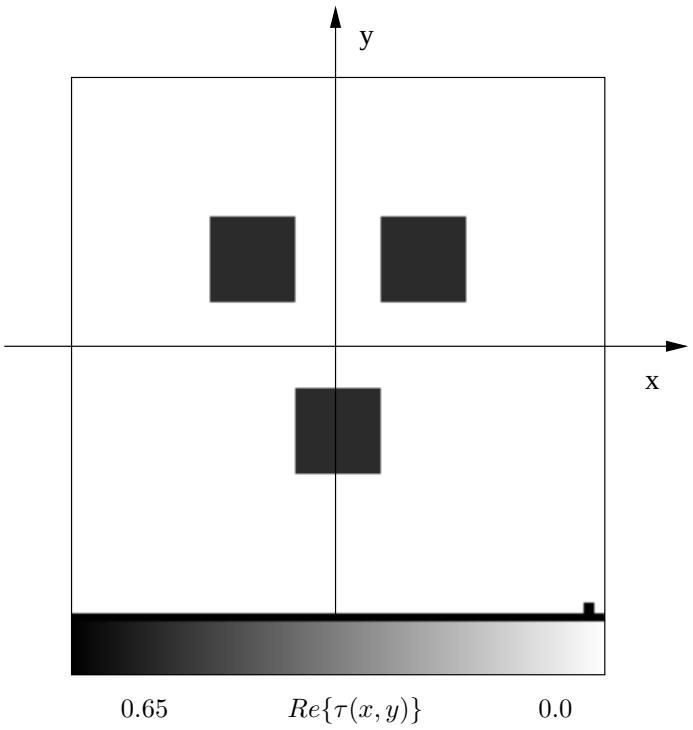

Figure 6 - D. Franceschini *et al.*, *"Iterative Image Reconstruction of ..."*

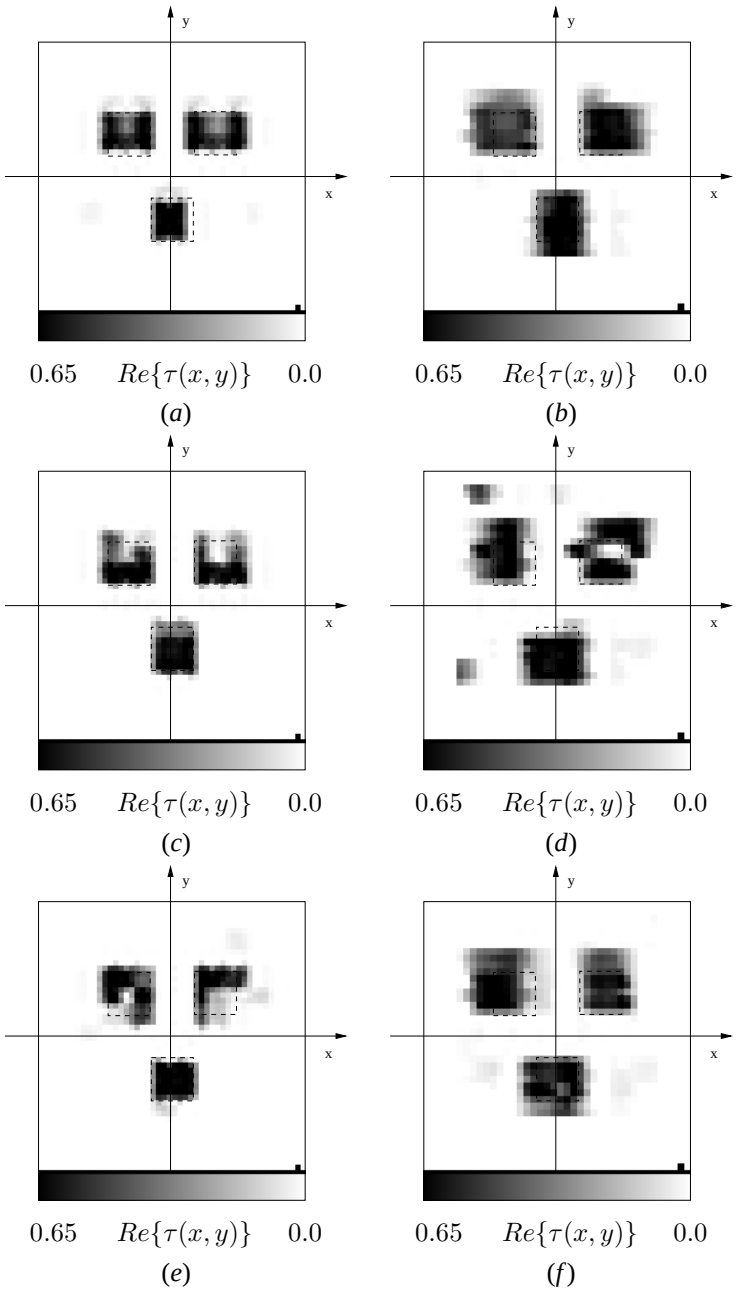

Figure 7 - D. Franceschini *et al.*, *"Iterative Image Reconstruction of ..."* .

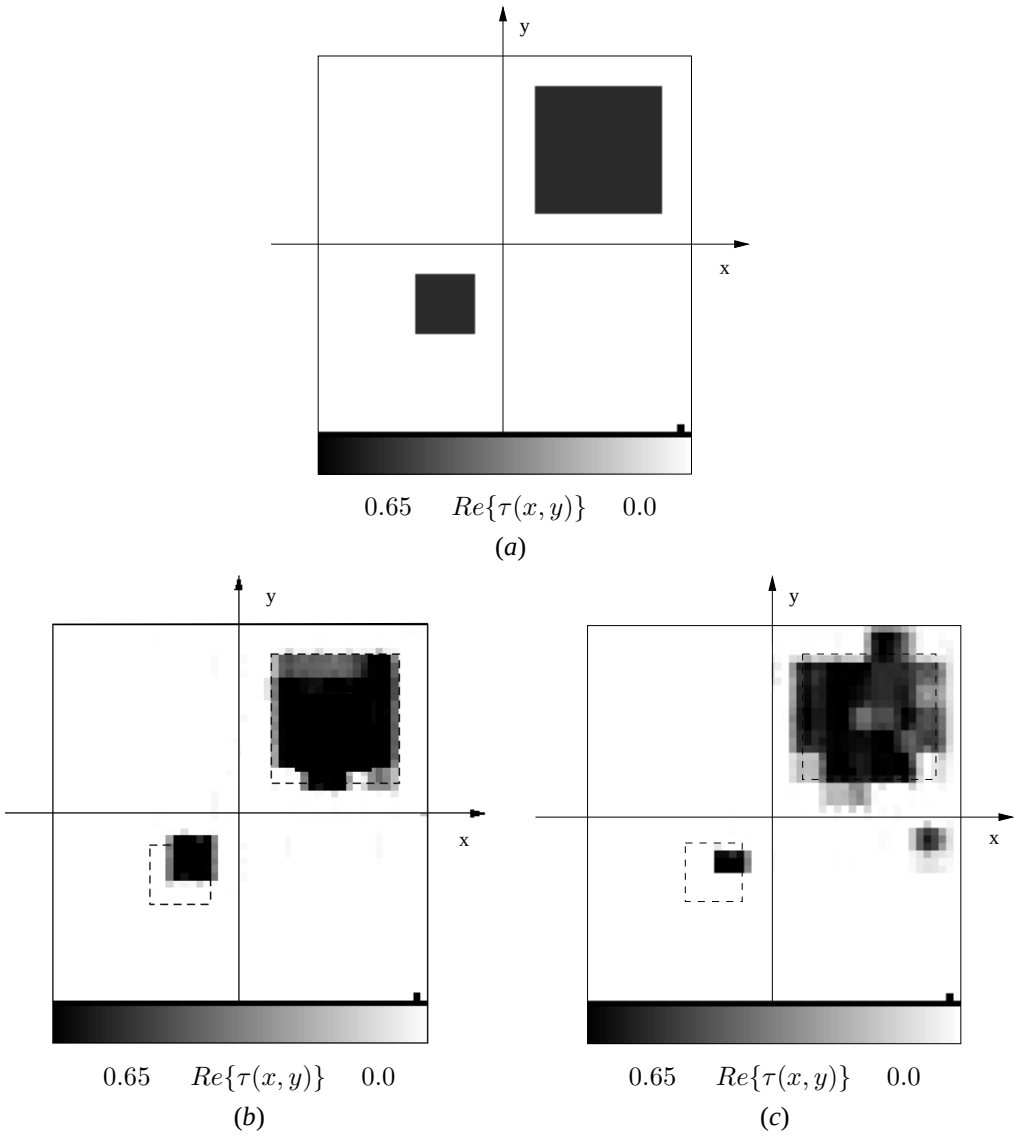

Figure 8 - D. Franceschini *et al.*, "*Iterative Image Reconstruction of ...*"

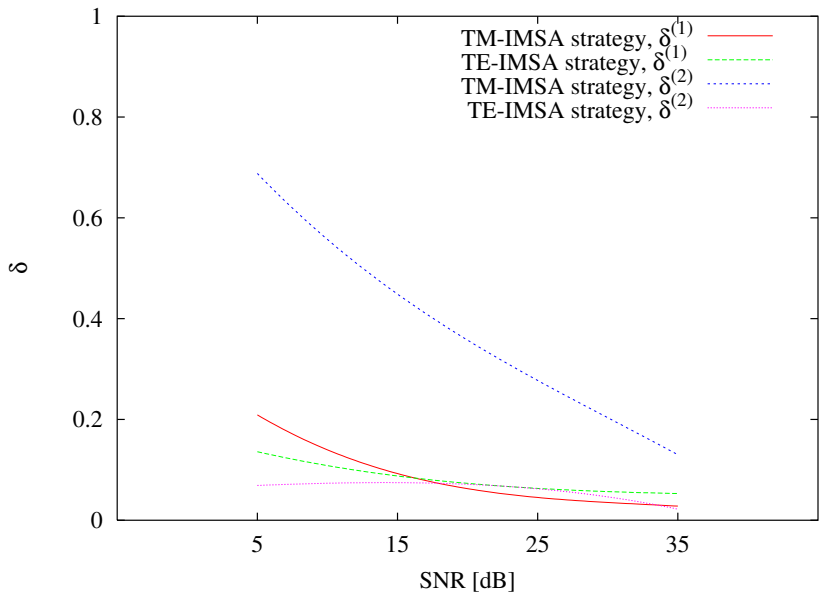

(*a*)

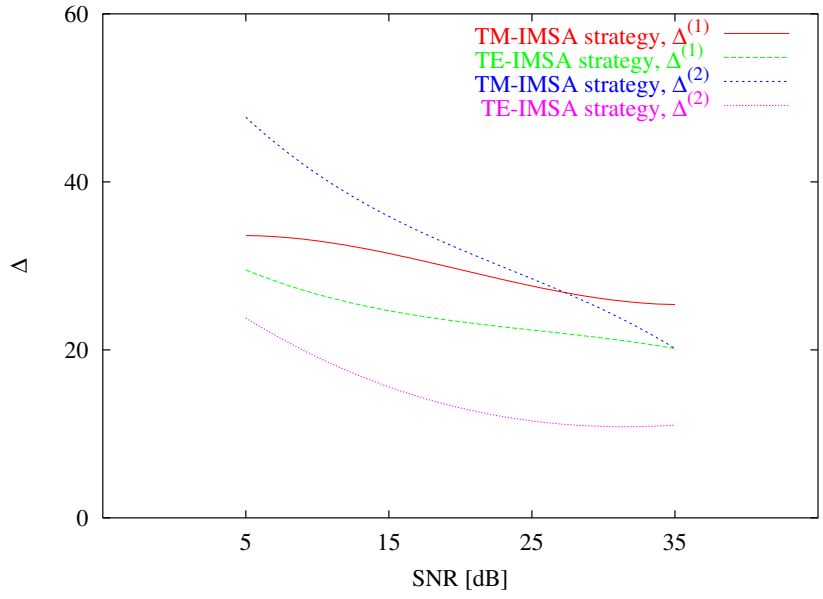

(*b*)

Figure 9(*I*) - D. Franceschini *et al.*, "*Iterative Image Reconstruction of ...*"

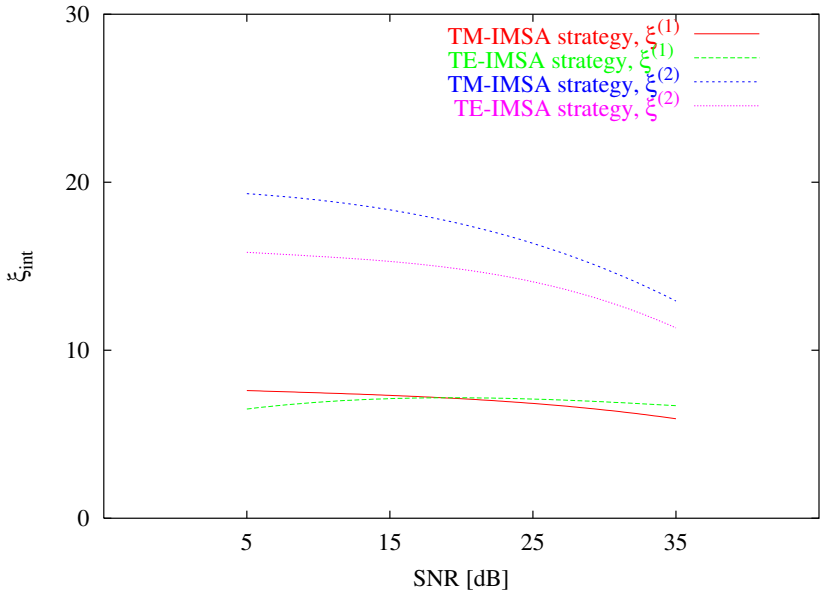

(*c*)

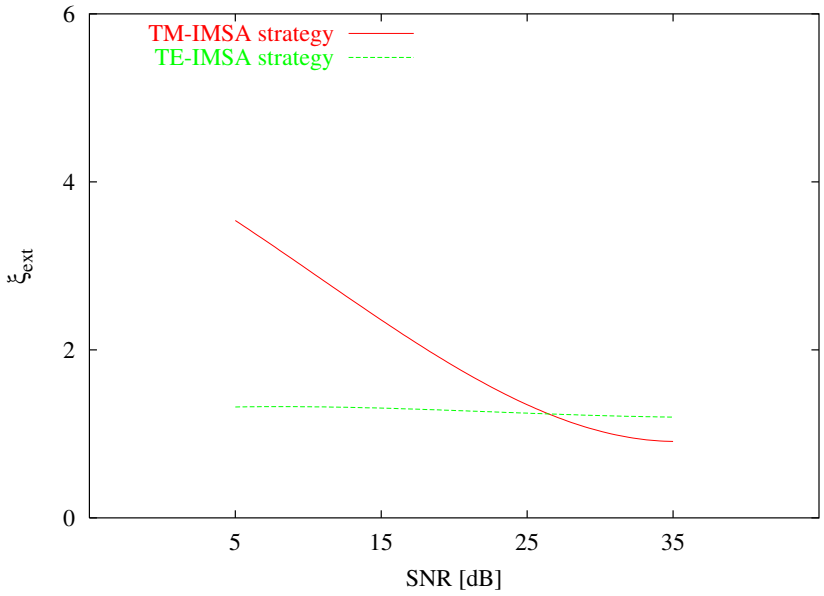

(*d*)

Figure 9(*II*) - D. Franceschini *et al.*, *"Iterative Image Reconstruction of ..."*

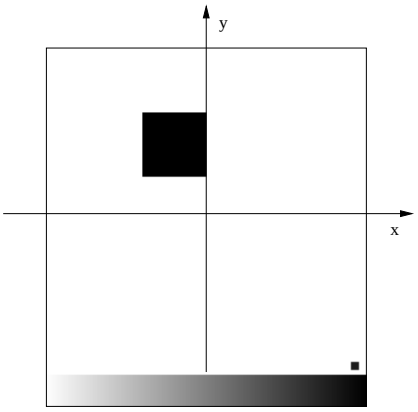

$0.0 \qquad Im\{\tau(x,y)\} \qquad -40.0$

(*a*)

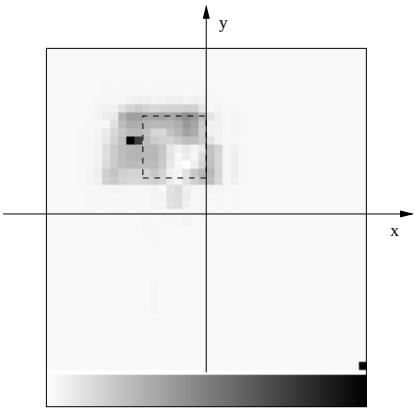

$0.0 \qquad Im\{\tau(x,y)\} \qquad -40.0$

(*b*)

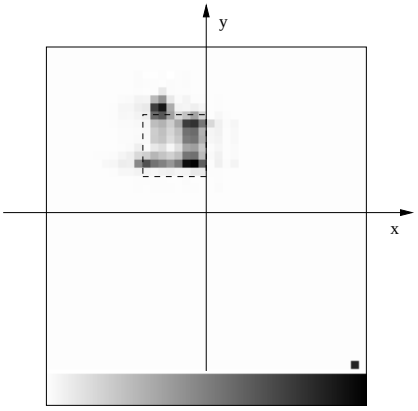

$0.0 \qquad Im\{\tau(x,y)\} \qquad -40.0$

(*c*)

Figure 10 - D. Franceschini *et al.*, *"Iterative Image Reconstruction of ..."*

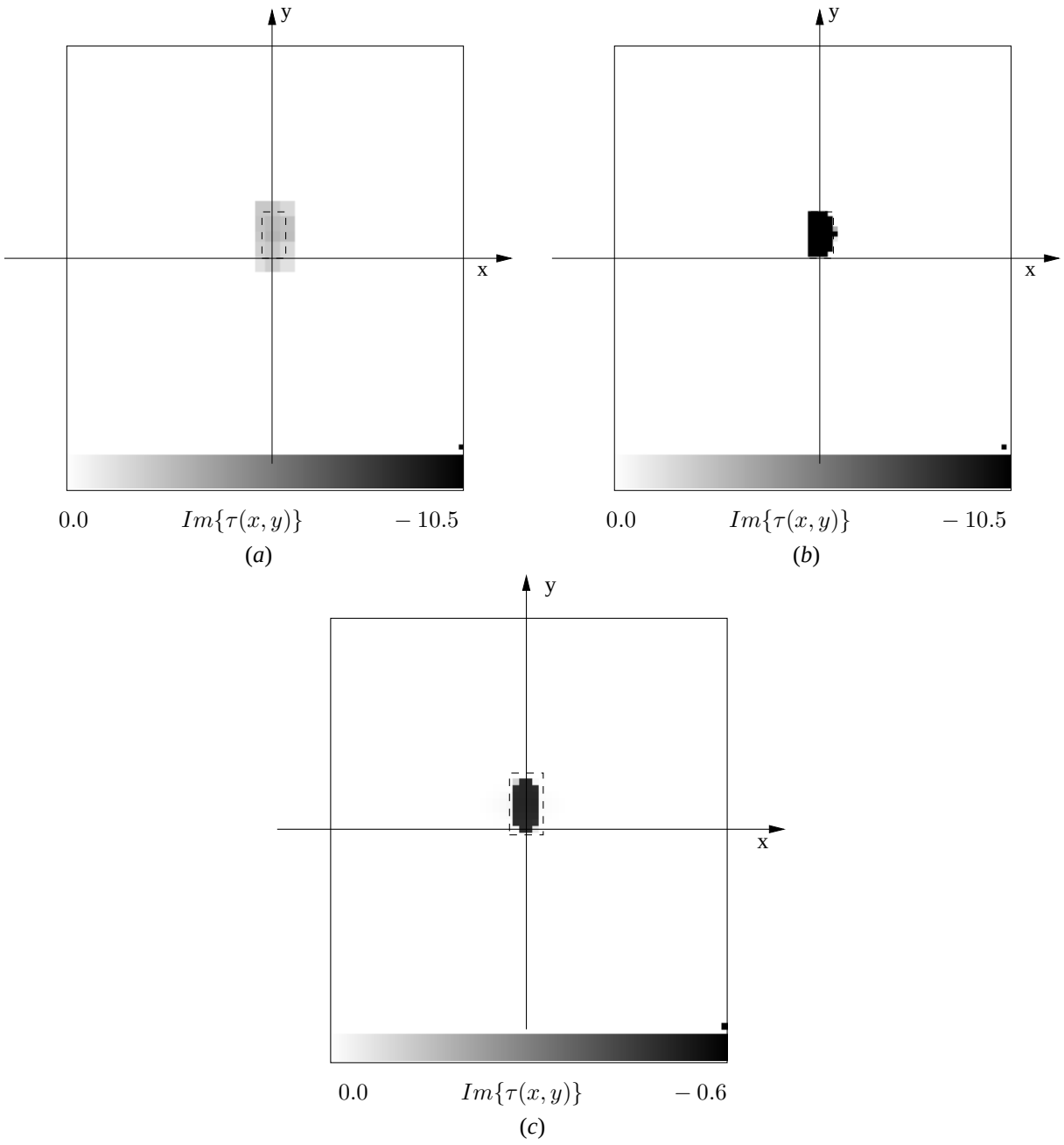

Figure 11 - D. Franceschini *et al.*, *"Iterative Image Reconstruction of ..."*

	TM	TE	TE_x	TE_y
ξ_{tot}	0.31	0.21	3.25	3.72
ξ_{int}	6.64	4.77	28.72	29.35
ξ_{ext}	0.43	0.02	1.32	1.91
δ	0.004	0.0002	0.32	0.30
Δ	14.44	12.33	27.32	27.57

Table I - D. Franceschini *et al.*, *" Iterative Image Reconstruction of ..."*

	TE	TM
K_{opt}	8000	1693
p_{opt}	4	2
t_{iter} $[ms]$	120	36
U $[MB]$	2.4	0.8

Table II - D. Franceschini *et al.,* "*Iterative Image Reconstruction of ...*"

$SNR \quad [dB]$	∞	10	5
ξ_{tot}	2.00	2.14	2.58
$\xi_{int}^{(1)}$	2.56	4.32	4.59
$\xi_{int}^{(2)}$	4.26	4.37	5.11
$\xi_{int}^{(3)}$	4.96	6.44	6.91
ξ_{ext}	1.21	1.43	1.72
$\delta^{(1)}$	0.02	0.05	0.01
$\delta^{(2)}$	0.02	0.05	0.05
$\delta^{(3)}$	0.01	0.05	0.10
$\Delta^{(1)}$	14.28	11.42	16.23
$\Delta^{(2)}$	14.41	13.46	11.44
$\Delta^{(3)}$	19.02	15.47	16.44

Table III - D. Franceschini *et al.,* " *Iterative Image Reconstruction of ...*"

$SNR \quad [dB]$	∞	10	5
ξ_{tot}	2.09	2.95	4.20
$\xi_{int}^{(1)}$	3.97	5.50	6.68
$\xi_{int}^{(2)}$	4.06	8.06	11.78
$\xi_{int}^{(3)}$	4.97	7.01	8.68
ξ_{ext}	1.77	2.60	4.17
$\delta^{(1)}$	0.01	0.02	0.03
$\delta^{(2)}$	0.04	0.04	0.08
$\delta^{(3)}$	0.01	0.04	0.07
$\Delta^{(1)}$	18.53	25.82	25.81
$\Delta^{(2)}$	13.58	26.70	27.41
$\Delta^{(3)}$	12.57	16.16	15.8

Table IV - D. Franceschini *et al.,* "*Iterative Image Reconstruction of ...*"

		SNR $[dB]$			
		∞	20	10	5
TE	K_{opt}	4000	6000	4000	4000
	p_{opt}	2	3	2	2
TM	K_{opt}	2309	4000	4000	6000
	p_{opt}	2	2	2	3

Table V - D. Franceschini *et al.*, *"Iterative Image Reconstruction of ..."*

$SNR\ \ 5dB$	TE	TM
$\xi_{int}^{(1)}$	6.50	7.60
$\xi_{int}^{(2)}$	15.83	19.32
ξ_{ext}	1.32	3.54
$\delta^{(1)}$	0.14	0.21
$\delta^{(2)}$	0.07	0.69
$\Delta^{(1)}$	29.52	33.60
$\Delta^{(2)}$	23.78	47.70

Table VI - D. Franceschini *et al.,* "*Iterative Image Reconstruction of ...*"

		SNR $[dB]$			
		∞	20	10	5
TE	K_{opt}	4000	5100	4000	4000
	p_{opt}	2	3	2	2
TM	K_{opt}	747	770	946	3790
	p_{opt}	2	2	2	3

Table VII - D. Franceschini *et al.,* "*Iterative Image Reconstruction of ...*"